THE JOURNAL OF PHYSICAL CHEMISTRY C

Article

Cite This: J. Phys. Chem. C 2018, 122, 20027−20033

pubs.acs.org/JPCC

Tuning the Photocatalytic Activity of $SrTiO_3$ by Varying the Sr/Ti Ratio: Unusual Effect of Viscosity of the Synthesis Medium

Harsha Bantawal,[†] U. Sandhya Shenoy,[‡] and D. Krishna Bhat*[,†]

[†]Department of Chemistry, National Institute of Technology Karnataka, Surathkal, Mangalore 575025, India

[‡]Department of Chemistry, College of Engineering and Technology, Srinivas University, Mukka, Mangalore 574146, India

Supporting Information

ABSTRACT: $SrTiO_3$ nanostructures were successfully synthesized in various alcohols as cosolvent as well as surfactant by a facile solvothermal method. The as-synthesized catalysts were characterized by X-ray diffraction technique, scanning electron microscopy, energy-dispersive X-ray analysis, Brunauer−Emmett−Teller analysis, diffuse reflectance spectroscopy, and photoluminescence spectroscopy. The possible formation mechanism of $SrTiO_3$ in the presence of these alcohols is discussed, and the effect of these alcohols on the structure, Sr/Ti atomic ratio, and optical properties is related to the photocatalytic activity. First principles calculations were made use of to determine the effect of defects on the electronic structure and the band gap. The photocatalytic activity of these catalysts was evaluated by taking methylene blue as a model pollutant under visible light irradiation. It was found that the photocatalytic activity of ethanol-mediated $SrTiO_3$ was found to be higher than the other samples because of the synergistic effect of high surface area and lesser defects.

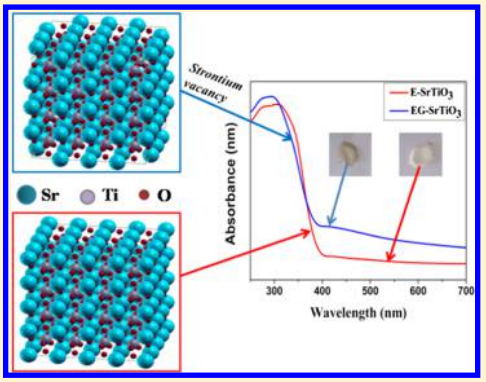

1. INTRODUCTION

Photocatalysis has gained widespread attention in the removal of recalcitrant pollutants present in water and air. Various semiconductor photocatalysts have been probed in recent years. Among them, TiO_2 is the most predominantly studied photocatalyst because of its outstanding photocatalytic activity, ease of preparation, and excellent stability. Perovskite alkaline earth titanates ($ATiO_3$, A = Ca, Ba, and Sr) are renowned semiconductor photocatalysts with compelling properties in ferroelectricity, superconductivity, catalysis, and so on.[1] Among them, $SrTiO_3$ is one of the well-known semiconductor photocatalysts because of its low cost, high chemical stability, and biocompatibility.[2] As compared to simple binary oxides, the physical and chemical properties of the multication oxide of $SrTiO_3$ can be suitably tuned by altering the compositions, and they also possess a large number of photocatalytic active sites.[3]

In general, the photocatalytic activity of a semiconductor photocatalyst mainly depends on its surface area, particle size, adsorbability, and defect chemistry.[4−7] The conventional synthesis of $SrTiO_3$ requires high temperature, which leads to severe agglomeration and formation of large particles, which results in poor photocatalytic activity. Solvothermal synthesis is one of the promising wet chemical methods to obtain $SrTiO_3$ nanostructures in which it is possible to tune the particle size and morphology, by tailoring various processing parameters such as surfactants, reaction temperature, reaction time, and solvents.[8−10] A large number of photocatalysts such as ZnO, Bi_2MoO_6, BiOBr, and $ZnIn_2S_4$ have been synthesized under solvothermal conditions and their morphology and size were properly tuned by employing different solvents in the earlier reports.[11−15] Wei et al. synthesized $SrTiO_3$ powders via the hydrothermal method by varying the concentration of poly(vinyl alcohol) (PVA) and found that for an intermediate concentration of PVA the photocatalytic activity was found to be higher. This was attributed to the synergistic effect of the specific surface area, Sr vacancy formation, and the adsorbability.[16] To the best of our knowledge, the effect of alcohols on the structure, morphology, Sr/Ti atomic ratio, and O vacancies of $SrTiO_3$ has never been investigated.

In view of these aspects, herein we synthesized $SrTiO_3$ by the solvothermal approach in different solvents, viz., butanol, ethanol, ethylene glycol, and propanol. The effect of these solvents on the structure, morphology, Sr/Ti atomic ratio, and photocatalytic activity was examined. In addition, the formation mechanism of $SrTiO_3$ nanostructures was also proposed. First principles density functional theory (DFT) calculations were used to determine the effect of defects on the electronic structure of $SrTiO_3$. The photocatalytic activities of these solvent-mediated $SrTiO_3$ photocatalysts were evaluated by the decomposition of methylene blue (MB) under visible light irradiation.

Received: July 8, 2018
Revised: August 13, 2018
Published: August 14, 2018

DOI: 10.1021/acs.jpcc.8b06514
J. Phys. Chem. C 2018, 122, 20027−20033

2. EXPERIMENTAL SECTION

2.1. Materials. All chemicals were of analytical grade and were used as procured without further purification. Titanium(IV) isopropoxide, strontium chloride, potassium hydroxide, butanol, ethylene glycol, and 2-propanol were procured from Sigma-Aldrich. Absolute ethanol was procured from Changshu Hongsheng Fine Chemical Co., Ltd.

2.2. Preparation of Catalyst. To prepare solution A, 1.47 mL of Titanium(IV) isopropoxide was dissolved in 10 mL of various solvents (butanol, ethanol, ethylene glycol, and 2-propanol). To prepare solution B, an appropriate amount of $SrCl_2$ was dissolved in 10 mL of 2 M KOH. Solution B was added dropwise to solution A with stirring. The resultant solution was sealed in an autoclave and kept in an oven maintained at 200 °C for 4 h. The obtained precipitate was washed with 1 M acetic acid and water to remove additional impurities. The washed products were dried in an oven at 70 °C for 8 h. The products obtained by using butanol, ethanol, ethylene glycol, and 2-propanol as cosolvents were designated as B-$SrTiO_3$, E-$SrTiO_3$, EG-$SrTiO_3$, and P-$SrTiO_3$, respectively.

2.3. Characterization. The structural characterization of the prepared catalysts was carried out using an X-ray diffractometer (Rigaku) with monochromatic Cu Kα radiation (λ = 0.154 nm) at a scan rate of 2° per minute in the range of 20°−70°. The surface morphology was analyzed using scanning electron microscopy (SEM) (Carl Zeiss) equipped with an energy-dispersive X-ray (EDX) analyzer (Oxford Instruments). The specific surface area was determined using the Brunauer−Emmett−Teller (BET) method (BEL SORP II, JAPAN) based on adsorption data in the relative pressure ranging from 0.05 to 0.03. The pore size distribution was determined using the Barrett−Joyner−Halenda (BJH) method applied to the desorption branch. The diffuse reflectance (DR) spectrum was obtained using a UV−visible spectrometer (Analytic Jena). The photoluminescence (PL) spectrum was recorded using a fluorescence spectrometer (Horiba JobinYvon).

2.4. Computational Details. DFT electronic structure calculations of stoichiometric and defective $SrTiO_3$ were carried out using the Quantum ESPRESSO package.[17] DFT calculations were performed using nonrelativistic Martins−Troullier norm-conserving pseudopotentials and the exchange-correlation energy functional of Perdew−Wang within a local density approximation.[18] The valence electrons of Sr ($5s^2$), Ti ($3d^24s^2$), and O ($2s^22p^4$) were included in the calculations through the use of pseudopotentials. $SrTiO_3$ is known to crystallize in a cubic perovskite structure with Sr occupying the corners of the cube, Ti at the center of the cube, and O at the face center. Simulations were carried out using a 2 × 2 × 1 supercell of $SrTiO_3$ containing 20 atoms. The systems were fully relaxed with respect to its lattice constant and atomic positions until the magnitude of the Hellman−Feynman force on each atom was less than 0.01 eV/Å and the magnitude of stresses was within 1 kbar. Plane wave basis sets used in the representation of wavefunctions and charge density were truncated at energy cutoffs of 80 and 320 Ry, respectively, to calculate the total energies. Self-consistent field (scf) calculations were performed using a 12 × 12 × 24 mesh of k points and a denser 24 × 24 × 48 mesh was used to sample Brillouin zone integrations for non-self-consistent field (nscf) calculations of the 2 × 2 × 1 supercell, respectively. Electronic structures were determined using a theoretical equilibrium lattice constant along high symmetry lines (Γ−X−M−Γ−R−X); (Γ−X−M−Γ−Z−R−A−Z) in the Brillouin zone, for a primitive unit cell and the 2 × 2 × 1 supercell, respectively.

2.5. Determination of Photocatalytic Activity. The photocatalytic activity of the prepared catalyst was determined by taking MB as a target pollutant under ambient atmospheric conditions. The photocatalytic reactor was equipped with a high-pressure 250 W Hg vapor lamp operating at a wavelength of 410−700 nm, which was used as a visible light source. In these experiments, 100 mL of MB solution (10 mg L^{-1}) and photocatalyst (50 mg) is taken in a 500 mL Pyrex glass beaker and magnetically stirred for 30 min in order to reach adsorption−desorption equilibrium. Then, the solution was irradiated with a visible light source. During photocatalytic studies, at regular intervals, 5 mL of the solution was sampled out, centrifuged, and the absorbance of the supernatant solution was measured using a UV−visible spectrometer at 664 nm. The percentage degradation of dye was calculated as per eq 1.

$$\text{Degradation } \% = [(C_o - C)/C_o] \times 100 \quad (1)$$

where C_o is the initial concentration of the solution and C is the concentration at different intervals of time.

3. RESULTS AND DISCUSSION

3.1. XRD Analysis. X-ray diffraction (XRD) analysis of the synthesized samples was carried out in order to examine the purity and crystal structure. Figure 1 shows the XRD pattern of

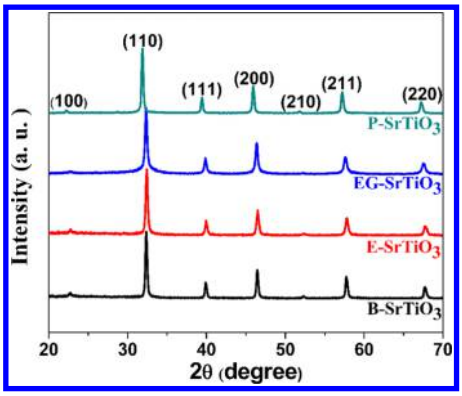

Figure 1. XRD pattern of the as-prepared catalysts in different solvents.

the as-prepared catalysts in different solvents. All the diffraction peaks are well matched to the cubic phase of $SrTiO_3$ (JCPDS card no. 00-040-1500), with lattice constants of $a = b = c$ = 3.9360 Å. No traces of other impurities were present. The average crystal sizes of the samples are in general calculated using the Scherrer equation, which uses the value of full width at half-maximum (FWHM).[19] It can be noted that the FWHM value of the (110) diffraction peaks decreased with decrease in the polarity of the solvents (Table 1). It can be noted that the average crystal size increases with decreasing the polarity of the solvents. This might be due to the aggregation of particles to larger sizes to acquire colloidal stability.[20]

3.2. SEM and EDX Analysis. In this work, the effect of different alcohols on the morphology of $SrTiO_3$ nanostructures is studied by keeping other experimental conditions same. Alcohols have been considered as a cosolvent and surfactant in

DOI: 10.1021/acs.jpcc.8b06514
J. Phys. Chem. C 2018, 122, 20027−20033

Table 1. Relative Polarity of Different Solvents

sl. no.	solvent	relative polarity
1	ethylene glycol	0.790
2	ethanol	0.654
3	butanol	0.586
4	2-propanol	0.546

hydrothermal reactions.[21] It is well known that the crystal growth is mainly dependent on diffusion kinetics. During the formation of a crystal, the reactant molecules initially diffuse from the bulk of the solution to the surface of the nucleus and then react with the nucleus. Generally, the shape of nanocrystals is mainly dependent on the concentration of the reactant molecules near the surface of a nucleus. High viscosity of solvents results in a low diffusion rate, which leads to the slow growth rate and isotropic generation of nanostructures whereas low viscosity of solvents results in a high diffusion rate, leading to a faster growth rate and anisotropic generation of nanostructures.[22]

The formation of $SrTiO_3$ nanostructures proceeds by diffusion of ions into the initially formed clusters. In ethylene glycol-mediated synthesis, because of the high viscosity of ethylene glycol, the concentration of the reactants near the nucleation site is less, which results in a slow growth rate and isotropic generation of nanostructures (Figure S1). The ethylene glycol medium can act not only as a solvent in the process but also as a stabilizer to control the crystal growth and prevent the agglomeration.[23] However, in low-viscosity solvents such as ethanol, 2-propanol, and butanol, the concentration of the reactants near the nucleation site is high, which results in a faster growth rate and anisotropic generation of nanostructures. On the basis of the above concept, the formation mechanisms are schematically shown in Figure 2.

The chemical composition of the $SrTiO_3$ nanostructures synthesized in different solvents was analyzed by EDX analysis as shown in Figure 3. The EDX analysis results revealed that the Sr/Ti atomic ratio of $SrTiO_3$ nanostructures synthesized in butanol, ethanol, ethylene glycol, and 2-propanol was found to be 0.91, 0.96, 0.73, and 0.90, respectively. This deviation in the nominal composition (Sr/Ti = 1) might be attributed to the formation of Sr vacancies during the formation of $SrTiO_3$ crystallites.[24]

3.3. Nitrogen Adsorption Analysis. The nitrogen adsorption−desorption isotherms were investigated in order to analyze the specific surface area and porosity of the synthesized $SrTiO_3$ nanostructures as shown in Figure S2. The isotherms of all the $SrTiO_3$ nanostructures were categorized as type IV according to the Brunauer−Deming−Deming−Teller classification with the hysteresis loops resembling type H3 at a relative pressure range of 0.4−1.0, indicating the presence of slitlike pores.[25] The BJH method was used to calculate the pore size distribution of the synthesized $SrTiO_3$ nanostructures. All the samples present a similar pore size distribution as shown in Figure S3. The mesopore size is primarily scattered in the range of 2−10 nm. The presence of such mesopores is believed to enhance the overall surface area, which in turn boosts the catalytic activity.[26] The textural properties of the $SrTiO_3$ nanostructures synthesized in different solvents are presented in Table 2.

3.4. Optical Absorbance Analysis. The optical properties of the as-synthesized $SrTiO_3$ nanostructures were investigated by DR spectroscopy. E-$SrTiO_3$ and P-$SrTiO_3$ nanostructures exhibited the absorption limit at 394 nm and B-$SrTiO_3$ at 400 nm, respectively (Figure 4). The corresponding band gap energy was found to be 3.14 and 3.1 eV.

In contrast, EG-$SrTiO_3$ exhibited a higher absorption beyond 400 nm with an absorption edge at 424 nm (band gap energy of 2.92 eV). The band gap energy was calculated from the absorption limit wavelength.[27] The extended absorption in the visible region can be attributed to the low Sr/Ti atomic ratio, which results in the formation of an O vacancy or Ti^{3+} defects for the charge compensation.[28]

3.5. Band Gap Analysis. To study the electronic properties, the atomic structure of stoichiometric $SrTiO_3$ was optimized initially using a primitive unit cell containing five atoms. A *k*-mesh of 24 × 24 × 24 and 48 × 48 × 48 for scf and nscf calculations was used, respectively. The obtained lattice constant of 3.813 Å was in good agreement with the

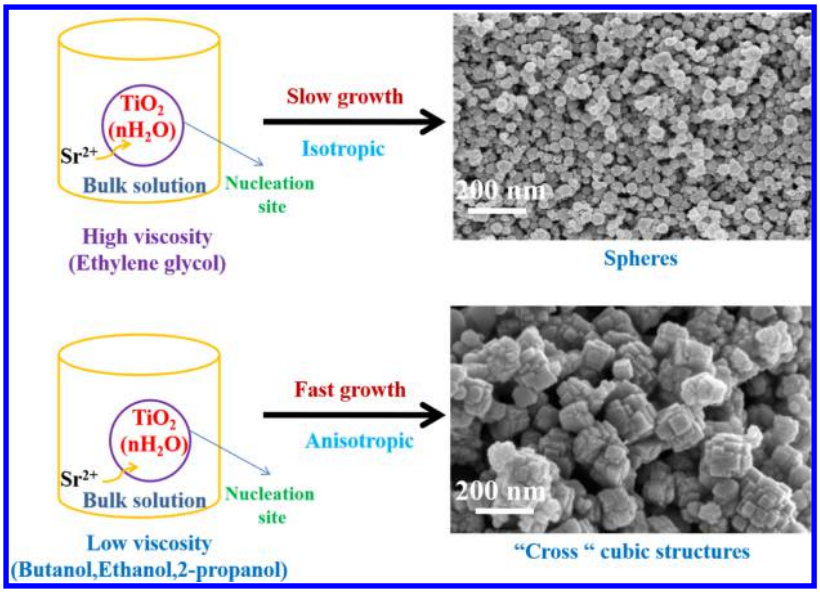

Figure 2. Possible formation mechanism of $SrTiO_3$ nanostructures synthesized in different solvents.

DOI: 10.1021/acs.jpcc.8b06514
J. Phys. Chem. C 2018, 122, 20027−20033

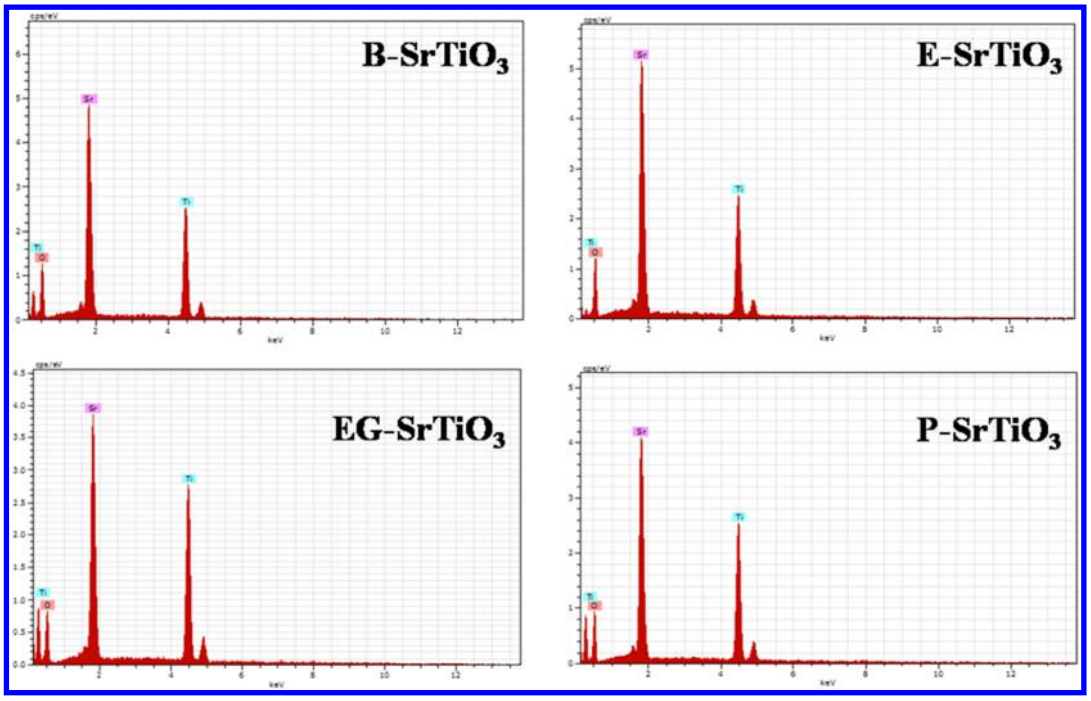

Figure 3. EDX traces of the $SrTiO_3$ nanostructures synthesized in different solvents.

Table 2. Textural Properties of the $SrTiO_3$ Nanostructures

sl. no.	catalyst	BET surface area (m^2/g)	pore diameter (nm)	pore volume (cm^3/g)
1	B-$SrTiO_3$	30.48	3.673	0.052
2	E-$SrTiO_3$	43.97	3.663	0.086
3	EG-$SrTiO_3$	83.35	3.399	0.130
4	P-$SrTiO_3$	26.45	3.657	0.061

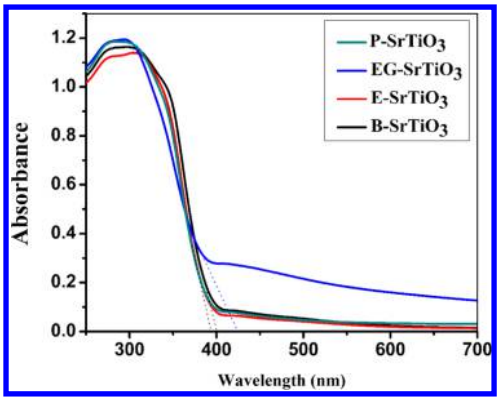

Figure 4. DR spectra of $SrTiO_3$ nanostructures synthesized in different solvents.

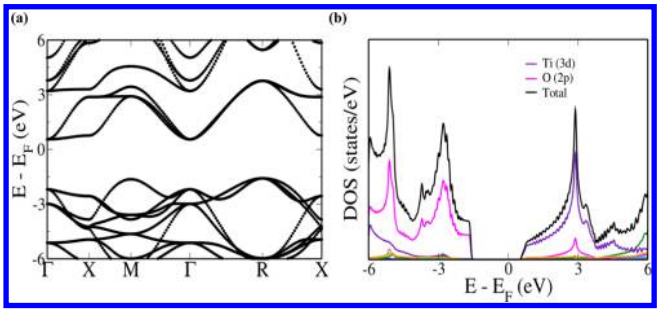

Figure 5. (a) Electronic structure and (b) pdos of a primitive unit cell of $SrTiO_3$.

experimental lattice constant, well within the typical DFT error. First principles calculations of the electronic structure of primitive $SrTiO_3$ (Figure 5a) show a direct band gap of 2.74 eV at the Γ point. The Fermi level lies within the band gap slightly closer to the conduction band. The top of the valence band lies at the *R* point and the bottom of the conduction band is at the Γ point, leading to an indirect band gap of 2.14 eV in comparison to the previously reported direct band gap of 2.34 eV and indirect band gap of 1.99 eV.[29] The deviation from the experimental band gap of 3.20 eV is due to the well-known underestimation in DFT. Partial density of states (pdos) shown in Figure 5b reveals that the valence band has a predominant O "2p" character, whereas the conduction band has a major contribution from Ti "3d" orbitals. The unoccupied Ti "d" orbitals and occupied O "p" orbitals induce "d" orbital n-type and "p" orbital p-type transport properties.[30]

As the electronic band gap is typically underestimated in DFT calculations, the Heyd−Scuseria−Ernzerhof (HSE-06) hybrid functional was used to obtain more accurate estimates of the band gap. A *k*-mesh of 12 × 12 × 12 and a *q*-mesh of 3 × 3 × 3 were used for the estimation. In Figure S4, it is seen that a band gap of 3.61 eV is obtained, which is comparable to the experimentally obtained band gap and is consistent with the value of 3.59 eV of the previously reported literature.[31] As HSE calculations are very expensive, standard DFT calculations are presented in the case of supercells, keeping in mind the underestimation of gaps, as the character of the band structure and band gap variations are expected to be reasonable and reliable. In order to study the effect of defects on the electronic structure and the band gap of $SrTiO_3$, defects were created in the supercell by creating a Sr and/or O vacancy. The electronic structure and density of states plot reveals that the band gap and the orbital contributions of the 2 × 2 × 1 supercell of stoichiometric $SrTiO_3$ are consistent with that of the simulated primitive unit cell (Figure S5). In order to create

DOI: 10.1021/acs.jpcc.8b06514
J. Phys. Chem. C 2018, 122, 20027−20033

a Sr vacancy, one Sr atom was removed from the supercell and the structure was fully relaxed. It is observed that the O atoms surrounding the vacancy (nearest neighbor) move away from the Sr vacancy site (Figure S6) and the Sr−O bond length decreases from 2.696 to 2.587 Å. While, the Ti−O bond length decreases from 1.907 to 1.879 Å when it bonds with O (shown in pink color) closer to two Sr vacancies and it increases to 1.913 Å when it bonds to O (shown in green color) closer to a single Sr vacancy and 1.947 Å when it bonds to O (shown in purple color) farther away from the vacancy. The electronic structure reveals a decrease in the direct band gap of 2.74 eV to 2.38 eV for the 2 × 2 × 1 supercell at the Γ point (Figure 6).

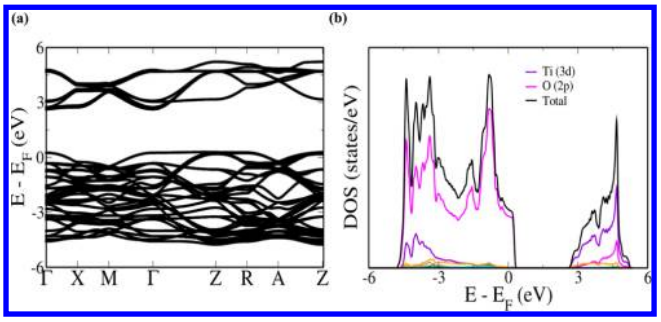

Figure 6. (a) Electronic structure and (b) pdos of the 2 × 2 × 1 supercell of $SrTiO_3$ with a single Sr vacancy.

The Fermi level moves into the valence band, indicating a p-type nature of the vacancy. To study the O vacancy, a single O atom was removed from the 2 × 2 × 1 supercell. The electronic structure revealed a Fermi level well within the conduction band, indicating an n-type nature.[30] The direct band gap appeared at the *Z* point and was found to decrease in this case to 1.95 eV (Figure 7). As it was reported earlier that

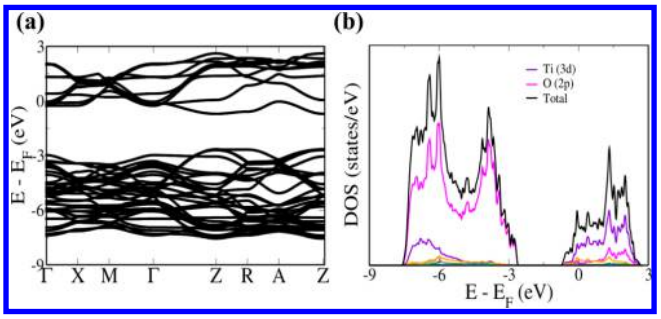

Figure 7. (a) Electronic structure and (b) pdos of the 2 × 2 × 1 supercell of $SrTiO_3$ with a single O vacancy.

complex defects with Sr and O vacancies have not been simulated by DFT, here a single Sr and O vacancy was introduced in the 2 × 2 × 1 supercell.[32] To create a Sr/O vacancy, removing any one of the Sr/O atoms from the 2 × 2 × 1 supercell would be sufficient as all Sr/O atoms are symmetry equivalent. However, there are several configurations of chemical ordering in which Sr and O vacancies can be formed simultaneously. Hence, the position of the Sr vacancy was fixed and then the position of O was determined. Out of several possibilities, there are only two configurations which are symmetry in-equivalent (Figure S7). The energies of both the configurations were calculated and the one with the lowest energy was considered in the present study. The electronic structure reveals a direct band gap of 1.79 eV at the *Z* point (Figure 8). Both these vacancies compensate each other, pushing the Fermi level into the band gap just above the valence band.

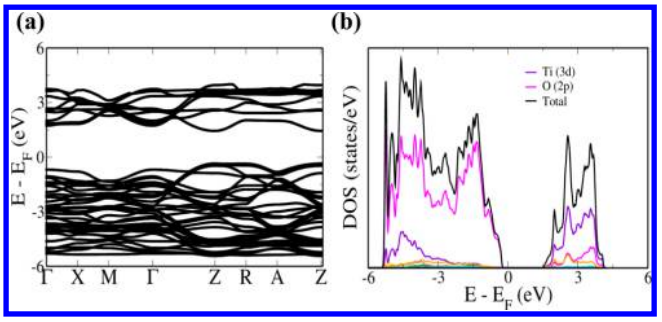

Figure 8. (a) Electronic structure and (b) pdos of the 2 × 2 × 1 supercell of $SrTiO_3$ with a single Sr and O vacancy.

3.6. PL Analysis. The PL spectra of the synthesized $SrTiO_3$ nanostructures were analyzed in order to get more insight into the O vacancies and electron hole recombination behavior. It is found that the $SrTiO_3$ synthesized in ethylene glycol had broad and intense PL emission in the blue region (450−500 nm) as shown in Figure S8, mainly because of the presence of O vacancies.[33] The presence of O vacancies or Ti^{3+} defects has been considered as a recombination center which reduces the photocatalytic activity.[34] As a result, the $SrTiO_3$ synthesized in ethylene glycol is expected to show poor photocatalytic activity as compared to other samples.

3.7. Photocatalytic Performance of $SrTiO_3$ Nanostructures. The photocatalytic activity of the as-prepared catalysts was evaluated by taking MB dye under visible light irradiation. A blank test was also carried out wherein the MB solution was taken without any catalyst. In this case, there was no significant degradation. Figure 9 shows the photocatalytic degradation of

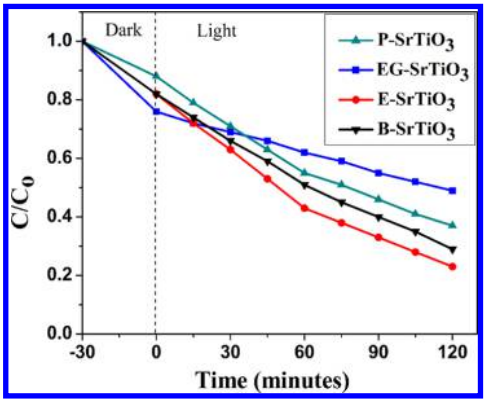

Figure 9. Degradation rates of MB by $SrTiO_3$ nanostructures synthesized in different solvents under visible light irradiation.

MB in the presence of $SrTiO_3$ synthesized in different solvents. The percentage degradation of B-$SrTiO_3$, EG-$SrTiO_3$, E-$SrTiO_3$, and P-$SrTiO_3$ was found to be 70.3, 50.9, 76, and 62.7, respectively. The photocatalytic activity of EG-$SrTiO_3$ was found to be less even though its surface area is greater than the other samples, which might be due to the presence of O vacancies or Ti^{3+} defects. These O vacancies have been considered as a recombination center for the photogenerated electrons. The photocatalytic activity of E-$SrTiO_3$ was found to be greater than other samples. This enhanced photocatalytic

DOI: 10.1021/acs.jpcc.8b06514
J. Phys. Chem. C 2018, 122, 20027−20033

activity is mainly due to the low recombination rate as well as high surface area. Further, the photocatalytic activity of B-$SrTiO_3$ and P-$SrTiO_3$ was found to be less than E-$SrTiO_3$, which might be due to the low surface area of the samples.

The kinetics of the photocatalytic degradation of MB (Figure S9) by the synthesized $SrTiO_3$ nanostructures is in accordance with the pseudo-first-order rate equation[35] as given in eq 2.

$$\ln(C/C_o) = -kt \quad (2)$$

where C_o is the concentration of the dye at time $t = 0$, C is the concentration of the dye at irradiation time (t), and k is the first-order rate constant, which was measured from the slope of the straight line. The rate constants for different $SrTiO_3$ nanostructures are shown in a bar diagram (Figure 10). It is found that the rate constant for E-$SrTiO_3$ is higher than all the prepared samples.

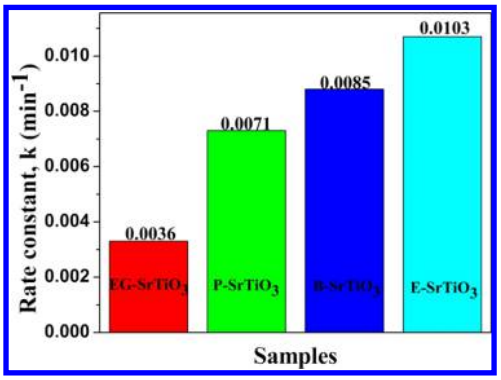

Figure 10. Rate constant k (min^{-1}) for the photodegradation of MB by $SrTiO_3$ nanostructures synthesized in different solvents under visible light irradiation.

The stability and reusability of catalysts is of great interest in the practical applications. E-$SrTiO_3$ was chosen to test the stability and recyclability. To evaluate the stability and reusability of the E-$SrTiO_3$, the photocatalytic activity was tested for four consecutive cycles by taking MB under visible light irradiation. It is found that there is only a slight decrease in the photocatalytic activity even after four cycles (Figure S10). This indicates that the E-$SrTiO_3$ is sufficiently stable for practical applications.

4. CONCLUSIONS

In summary, $SrTiO_3$ nanostructures were successfully synthesized by a facile solvothermal method in various alcohols, which served both as cosolvent and surfactant. It is found that the ethylene glycol-mediated synthesis resulted in isotropic generation of $SrTiO_3$ because of the high viscosity and low diffusion rate of reactants, which also led to a high surface area of 83.35 m^2/g, whereas ethanol-, 2-propanol-, and butanol-mediated synthesis resulted in anisotropic generation of $SrTiO_3$ because of the faster diffusion rate of the reactants. The EDX analysis results revealed the Sr/Ti atomic ratio of EG-$SrTiO_3$ nanostructures to be 0.73, which in turn resulted in the formation of an O vacancy or Ti^{3+} defects for the charge compensation. This was also confirmed by DR and PL spectroscopic techniques. First principles calculations revealed a decrease in the band gap in the presence of defects. The photocatalytic activity of E-$SrTiO_3$ was found to be greater than that of the other samples. This enhanced photocatalytic activity is mainly due to the absence of O vacancies as well as high surface area. The E-$SrTiO_3$ exhibited sufficient photocatalytic stability even after four cycles. Thus, the study shows that the nature of alcohols used as medium for the synthesis has a profound effect on the structural features and catalytic activity of materials.

■ ASSOCIATED CONTENT

Supporting Information

The Supporting Information is available free of charge on the ACS Publications website at DOI: 10.1021/acs.jpcc.8b06514.

FESEM images of $SrTiO_3$ nanostructures, nitrogen adsorption−desorption isotherms, BJH pore size distribution, pdos of primitive unit cell of $SrTiO_3$ simulated using HSE calculations, electronic structure and pdos of 2 × 2 × 1 supercell of $SrTiO_3$, crystal structure of the 2 × 2 × 1 supercell's various configurations, PL spectra, kinetics of the photocatalytic degradation of MB, and reusability of E-$SrTiO_3$ catalyst for the degradation of MB (PDF)

■ AUTHOR INFORMATION

Corresponding Author

*E-mail: denthajekb@gmail.com.

ORCID

D. Krishna Bhat: 0000-0003-0383-6017

Notes

The authors declare no competing financial interest.

■ ACKNOWLEDGMENTS

H.B. is thankful to the National Institute of Technology Karnataka Surathkal, Mangalore, for providing financial support in the form of Institute fellowship along with essential facilities to carry out this research work.

■ REFERENCES

(1) Wang, Y.; Niu, C.-G.; Wang, L.; Wang, Y.; Zhang, X.-G.; Zeng, G.-M. Synthesis of fern-like Ag/AgCl/CaTiO3 plasmonic photocatalysts and their enhanced visible-light photocatalytic properties. *RSC Adv.* **2016**, *6*, 47873−47882.

(2) Liu, J.; Zhang, L.; Li, N.; Tian, Q.; Zhou, J.; Sun, Y. Synthesis of MoS2/SrTiO3 composite materials for enhanced photocatalytic activity under UV irradiation. *J. Mater. Chem. A* **2015**, *3*, 706−712.

(3) Tan, B.; Toman, E.; Li, Y.; Wu, Y. Zinc Stannate (Zn2SnO4) Dye-sensitized solar cells. *J. Am. Chem. Soc.* **2007**, *129*, 4162−4163.

(4) Ahuja, S.; Kutty, T. R. N. Nanoparticles of SrTiO3 prepared by gel to crystallite conversion and their photocatalytic activity in the mineralization of phenol. *J. Photochem. Photobiol., A* **1996**, *97*, 99−107.

(5) Baiju, K. V.; Shukla, S.; Sandhya, K. S.; James, J.; Warrier, K. G. K. Photocatalytic Activity of Sol−Gel-Derived Nanocrystalline Titania. *J. Phys. Chem. C* **2007**, *111*, 7612−7622.

(6) Wang, Y.; Wang, Y.; Meng, Y.; Ding, H.; Shan, Y.; Zhao, X.; Tang, X. A Highly Efficient Visible-Light-Activated Photocatalyst Based on Bismuth- and Sulfur-Codoped TiO2. *J. Phys. Chem. C* **2008**, *112*, 6620−6626.

(7) Tran, T. H.; Nosaka, A. Y.; Nosaka, Y. Adsorption and Photocatalytic Decomposition of Amino Acids in TiO2Photocatalytic Systems†. *J. Phys. Chem. B* **2006**, *110*, 25525−25531.

(8) Qingqing, W.; Gang, X.; Gaorong, H. Solvothermal synthesis and characterization of uniform CdS nanowires in high yield. *J. Solid State Chem.* **2005**, *178*, 2680−2685.

DOI: 10.1021/acs.jpcc.8b06514
J. Phys. Chem. C 2018, 122, 20027−20033

(9) Zou, G.; Li, H.; Zhang, Y.; Xiong, K.; Qian, Y. Solvothermal/hydrothermal route to semiconductor nanowires. *Nanotechnology* **2006**, *17*, S313−S320.
(10) Demazeau, G. Solvothermal processes: new trends in Materials Chemistry. *J. Phys.: Conf. Ser.* **2008**, *121*, 082003.
(11) Hu, Q. R.; Wang, S. L.; Jiang, P.; Xu, H.; Zhang, Y.; Tang, W. H. Synthesis of ZnO nanostructures in organic solvents and their photoluminescence properties. *J. Alloys Compd.* **2010**, *496*, 494−499.
(12) Mi, Y.; Zeng, S.; Li, L.; Zhang, Q.; Wang, S.; Liu, C.; Sun, D. Solvent directed fabrication of Bi2WO6 nanostructures with different morphologies: Synthesis and their shape-dependent photocatalytic properties. *Mater. Res. Bull.* **2012**, *47*, 2623−2630.
(13) Xiong, X.; Ding, L.; Wang, Q.; Li, Y.; Jiang, Q.; Hu, J. Synthesis and photocatalytic activity of BiOBr nanosheets with tunable exposed {0 1 0} facets. *Appl. Catal., B* **2016**, *188*, 283−291.
(14) Fang, F.; Chen, L.; Chen, Y.-B.; Wu, L.-M. Synthesis and Photocatalysis of ZnIn2S4 Nano/Micropeony. *J. Phys. Chem. C* **2010**, *114*, 2393−2397.
(15) Xu, L.; Hu, Y.-L.; Pelligra, C.; Chen, C.-H.; Jin, L.; Huang, H.; Sithambaram, S.; Aindow, M.; Joesten, R.; Suib, S. L. ZnO with different morphologies synthesized by solvothermal methods for enhanced photocatalytic activity. *Chem. Mater.* **2009**, *21*, 2875−2885.
(16) Wei, X.; Xu, G.; Ren, Z.; Xu, C.; Shen, G.; Han, G. PVA-Assisted Hydrothermal Synthesis of SrTiO3Nanoparticles with Enhanced Photocatalytic Activity for Degradation of RhB. *J. Am. Ceram. Soc.* **2008**, *91*, 3795−3799.
(17) Giannozzi, P.; Baroni, S.; Bonini, N.; Calandra, M.; Car, R.; Cavazzoni, C.; Ceresoli, D.; Chiarotti, G. L.; Cococcioni, M.; Dabo, I.; et al. QUANTUM ESPRESSO: a modular and open-source software project for quantum simulations of materials. *J. Phys.: Condens. Matter* **2009**, *21*, 395502.
(18) Perdew, J. P.; Wang, Y. Accurate and simple analytic representation of the electron-gas correlation energy. *Phys. Rev. B: Condens. Matter Mater. Phys.* **1992**, *45*, 13244−13249.
(19) Sadiq, M. M. J.; Shenoy, U. S.; Bhat, D. K. Novel RGO-ZnWO4-Fe3O4 nanocomposite as high performance visible light photocatalyst. *RSC Adv.* **2016**, *6*, 61821−61829.
(20) Tiwari, A.; Wang, R.; Wei, B. *Advanced Surface Engineering Materials*; John Wiley and Sons: Canada, 2016.
(21) Dong, L.; Shi, H.; Cheng, K.; Wang, Q.; Weng, W.; Han, W. Shape-controlled growth of SrTiO3 polyhedral submicro/nanocrystals. *Nano Res.* **2014**, *7*, 1311−1318.
(22) Li, G.; Ding, Y.; Zhang, Y.; Lu, Z.; Sun, H.; Chen, R. Microwave synthesis of BiPO4 nanostructures and their morphology-dependent photocatalytic performances. *J. Colloid Interface Sci.* **2011**, *363*, 497−503.
(23) Sun, C.; Rajasekhara, S.; Goodenough, J. B.; Zhou, F. Monodisperse Porous LiFePO4Microspheres for a High Power Li-Ion Battery Cathode. *J. Am. Chem. Soc.* **2011**, *133*, 2132−2135.
(24) Xu, G.; Huang, X.; Zhang, Y.; Deng, S.; Wei, X.; Shen, G.; Han, G. Self-assembly and formation mechanism of single-crystal SrTiO3 nanosheets via solvothermal route with ethylene glycol as reaction medium. *CrystEngComm* **2013**, *15*, 7206−7211.
(25) Xiang, Q.; Yu, J.; Jaroniec, M. Enhanced photocatalytic H2-production activity of graphene-modified titania nanosheets. *Nanoscale* **2011**, *3*, 3670−3678.
(26) Sadiq, M. M. J.; Shenoy, U. S.; Bhat, D. K. NiWO 4 -ZnO-NRGO ternary nanocomposite as an efficient photocatalyst for degradation of methylene blue and reduction of 4-nitro phenol. *J. Phys. Chem. Solids* **2017**, *109*, 124−133.
(27) Wang, W.; Wang, Z.; Liu, J.; Luo, Z.; Suib, S. L.; He, P.; Ding, G.; Zhang, Z.; Sun, L. Single-step one-pot synthesis of TiO_2 nanosheets doped with sulfur on reduced graphene oxide with enhanced photocatalytic activity. *Sci. Rep.* **2017**, *7*, 46610.
(28) Sulaeman, U.; Yin, S.; Sato, T. Effect of Sr/Ti ratio on the photocatalytic properties of SrTiO3. *IOP Conf. Ser.: Mater. Sci. Eng.* **2011**, *18*, 032018.
(29) Jiao, S.; Yan, J.; Sun, G.; Zhao, Y. Electronic structures and optical properties of Nb-doped SrTiO3 from first principles. *Semiconductors* **2016**, *37*, 072001.
(30) Liao, X.-X.; Wang, H.-Q.; Zheng, J.-C. Tuning the structural, electronic, and magnetic properties of strontium titanate through atomic design: a comparison between oxygen vacancies and nitrogen doping. *J. Am. Ceram. Soc.* **2013**, *96*, 538−543.
(31) El-Mellouhi, F.; Brothers, E. N.; Lucero, M. J.; Scuseria, G. E. Modeling of the cubic and antiferro distortive phases of SrTiO3 with screened hybrid density functional theory. *Phys. Rev. B: Condens. Matter Mater. Phys.* **2011**, *84*, 115122.
(32) Kim, H.; Zhang, J. Y.; Raghavan, S.; Stemmer, S. Direct Observation of Sr vacancies in SrTiO3 by quantitative scanning transmission electron microscopy. *Phys. Rev. X* **2016**, *6*, 041063.
(33) Sarkar, T.; Ghosh, S.; Annamalai, M.; Patra, A.; Stoerzinger, K.; Lee, Y.-L.; Prakash, S.; Motapothula, M. R.; Shao-Horn, Y.; Giordano, L.; Venkatesan, T. The effect of oxygen vacancies on water wettability of transition metal based SrTiO3 and rare-earth based Lu2O3. *RSC Adv.* **2016**, *6*, 109234−109240.
(34) Liu, M.; Qiu, X.; Miyauchi, M.; Hashimoto, K. Cu(II) Oxide Amorphous Nanoclusters Grafted Ti3+Self-Doped TiO2: An Efficient Visible Light Photocatalyst. *Chem. Mater.* **2011**, *23*, 5282−5286.
(35) Mohamed, M. J. S.; Shenoy, U. S.; Bhat, D. K. Novel NRGO-CoWO4-Fe2O3 nanocomposite as an efficient catalyst for dye degradation and reduction of 4-nitrophenol. *Mater. Chem. Phys.* **2018**, *208*, 112−122.

DOI: 10.1021/acs.jpcc.8b06514
J. Phys. Chem. C 2018, 122, 20027−20033